

---

# A Robust Computational Framework for Estimating 3D Bi-Atrial Chamber Wall Thickness

Yufeng Wang, Zhaohan Xiong, Aaqel Nalar, Brian J. Hansen, Sanjay Kharche, Gunnar Seemann, Axel Loewe, Vadim V. Fedorov, Jichao Zhao\*

**Abstract**—Atrial fibrillation (AF) is the most prevalent form of cardiac arrhythmia. The atrial wall thickness (AWT) can potentially improve our understanding of the mechanism underlying atrial structure that drives AF and provides important clinical information. However, most existing studies for estimating AWT rely on ruler-based measurements performed on only a few selected locations in 2D or 3D using digital calipers. Only a few studies have developed automatic approaches to estimate the AWT in the left atrium, and there are currently no methods to robustly estimate the AWT of both atrial chambers. Therefore, we have developed a computational pipeline to automatically calculate the 3D AWT across bi-atrial chambers and extensively validated our pipeline on both *ex vivo* and *in vivo* human atria data. The atrial geometry was first obtained by segmenting the atrial wall from the MRIs using a novel machine learning approach. The epicardial and endocardial surfaces were then separated using a multi-planar convex hull approach to define boundary conditions, from which, a Laplace equation was solved numerically to automatically separate bi-atrial chambers. To robustly estimate the AWT in each atrial chamber, coupled partial differential equations by coupling the Laplace solution with two surface trajectory functions were formulated and solved. Our pipeline enabled the reconstruction and visualization of the 3D AWT for bi-atrial chambers with a relative error of 8% and outperformed existing algorithms by >7%. Our approach can potentially lead to improved clinical diagnosis, patient stratification, and clinical guidance during ablation treatment for patients with AF.

**Index Terms**—Atrial fibrillation, atrial wall thickness, Laplace solution, human atria, MRI

## I. INTRODUCTION

Atrial fibrillation (AF), leading to an irregular and rapid heart rate, is the most common sustained heart rhythm disturbance [1]. AF is associated with substantial morbidity and mortality, causing 1 out of 5 strokes in people aged over 60 years. The current overall prevalence of AF is ~2% in industrialized countries and is projected to more than double in the following decades [1, 2]. Current clinical treatments for AF

[3-5] perform poorly due to a lack of basic understanding of the underlying atrial anatomical structures which directly sustain AF.

AF, and especially persistent AF, is driven by complex substrates, which are widely distributed throughout both atrial chambers [3, 6, 7]. Repeated episodes of AF produce further changes in the structural properties of the atria, i.e., atrial structural remodeling (dilatation, myofiber changes, and fibrosis) [5, 6]. Atrial wall thickness (AWT) variation is demonstrated to have an important role in AF arrhythmogenesis as it influences the electrical activation patterns during episodes of AF, particularly in the right atrium (RA) [6, 8-12]. AWT can also play an important role in aiding the selection of regions to target and in planning radiofrequency power safety during ablation [13-15]. As a result, direct study of the atrial structure in patients with AF is vital, and accurate 3D AWT maps which visualize and characterize alternations caused by remodeling can potentially aid the understanding and treatment of AF.

Measuring AWT is a challenging task due to the high variability in the atrial morphology and regional wall thicknesses (0.4 to 11.7 mm), as well as the low resolution of current imaging methodologies, i.e., ~0.16 mm for *ex vivo* and ~0.625 mm for *in vivo* MRIs [6]. Most existing studies for estimating AWT rely on ruler-based measurements using digital calipers on 2D image slices, limiting the estimation to a few selected locations [8]. There are some existing studies developing different methods of automatic thickness estimation in various research fields [13-16]. These mostly involve surface-based methods such as measuring the nearest distance between the epicardial and endocardial surfaces [16-18] or using the lengths of the vectors normal to the epicardial surface which extends to the adjacent endocardium. More robust algorithms have been proposed, such as the center surface method which measures the distance between the epicardial and endocardial surfaces from a calculated center surface. However, the measurements of these surface-based approaches are still heavily reliant on the atrial surface geometry [19-21]. More

This work was supported by the National Heart Foundation of New Zealand and the Health Research Council of New Zealand (JZ), and National Institutes of Health grants HL115580 and HL135109 (VVF). *Asterisk indicates corresponding author.*

Y. Wang, Z. Xiong, A. Nalar and J. Zhao\* are with the Auckland Bioengineering Institute, The University of Auckland, Auckland, 1142, New Zealand (e-mail: j.zhao@auckland.ac.nz).

B. Hansen and V. Fedorov are with Department of Physiology and Cell Biology, The Ohio State University Wexner Medical Center, Columbus, USA.

S. Kharche is with Department of Medical Biophysics, Western University, Canada.

G. Seemann is with the Institute for Experimental Cardiovascular Medicine, University Heart Center Freiburg • Bad Krozingen, and the Faculty of Medicine, Albert-Ludwigs University, Freiburg, Germany.

A. Loewe is with the Institute of Biomedical Engineering, Karlsruhe Institute of Technology, Karlsruhe, Germany.

recently, a few studies have proposed advance image-based approaches for estimating the left atrial (LA) wall thickness [8, 9, 18, 22, 23]. Laplace-based solutions [9] generate a smooth set of non-intersecting field lines between two boundaries in space and are ideal for modeling the non-constant and highly variable epicardial and endocardial surfaces of the atria. The AWT can be estimated by the length of the trajectories along the direction of the gradient field between the two surfaces. When compared with the methods above, this approach is more robust as it accounts for the variation in geometry throughout the atrial walls. However, this approach still requires explicitly calculating gradient and distance trajectories which are time-consuming and error-prone. More importantly, to date, there are no studies or approaches for robust estimation of the AWT in both atrial chambers since AF is a bi-atrial chamber disease [8].

In this paper, we propose and evaluate a novel pipeline for automatically calculating 3D AWT in both atrial chambers from clinical images using a coupled partial differential equation (PDE) approach by coupling the Laplace solution with two surface trajectory functions. Our method is validated against several algorithms previously proposed for AWT in LA. This development is a very important step towards patient-specific diagnostics and treatment of AF, and could potentially improve our understanding of the atrial structures that sustain AF.

## II. METHODS

This section outlines the data and methods used in this study. The acquisition of the human atria data and the extraction of the atrial geometry are first described. A convex hull method for separating the atrial epicardial and endocardial surfaces from the atrial walls is then described, followed by the automatic separation of the LA and RA chambers by solving the Laplace equation. Various AWT estimation algorithms are then outlined, along with the proposed coupled PDE approach. A visualization of our proposed pipeline for calculating the 3D AWT from raw medical images is shown in Fig. 1.

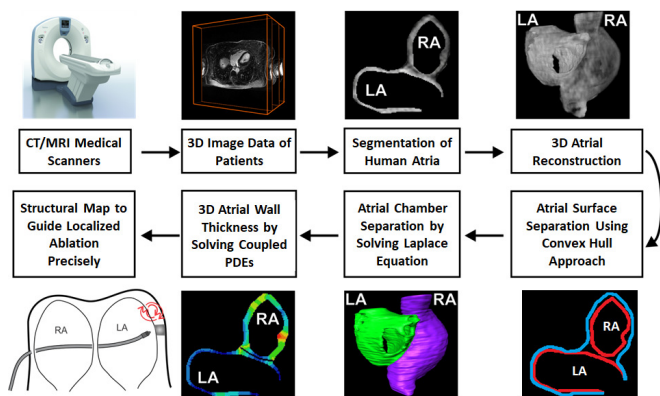


Fig. 1. Outline of framework for the computation of 3D atrial wall thickness (AWT) from 3D clinical image data. PDE, partial differential equation.

### A. Image Acquisition and Atrial Geometry Segmentation

One *ex vivo* post-mortem and two *in vivo* human atrial data were used in this study. The *ex vivo* data were obtained from a 59-year-old female patient using cryosection (the Visible Female dataset) with an isotropic resolution of  $0.33 \times 0.33 \times 0.33 \text{ mm}^3$ .

It was segmented manually based on the anatomical features defined in previous studies (Fig. 2A) [24, 25]. The two *in vivo* data (#1, 74 years old male, and #2, 59 years old female) with a spatial resolution of  $0.625 \times 0.625 \times 1.25 \text{ mm}^3$  were late gadolinium enhanced (LGE)-MRIs from patients with AF before ablation from The University of Utah [26]. The LGE-MRIs were obtained by using either a 1.5 Tesla Avanto or a 3.0 Tesla Verio clinical scanner (Siemens Medical Solutions, Erlangen, Germany). The whole atrial anatomical geometry was obtained automatically via a deep learning method [27] by segmenting the atrial walls of each LGE-MRI in a slice-by-slice manner to reconstruct the overall 3D atrial geometry (Fig. 2B). The deep learning method consisted of a multi-scaled, dual pathway convolutional neural network that captured both the local atrial tissue geometry and the global positional information of atria simultaneously. The approach was trained and validated on 154 LGE-MRIs, and was shown to produce high-quality 3D segmentation of the atrial geometries.

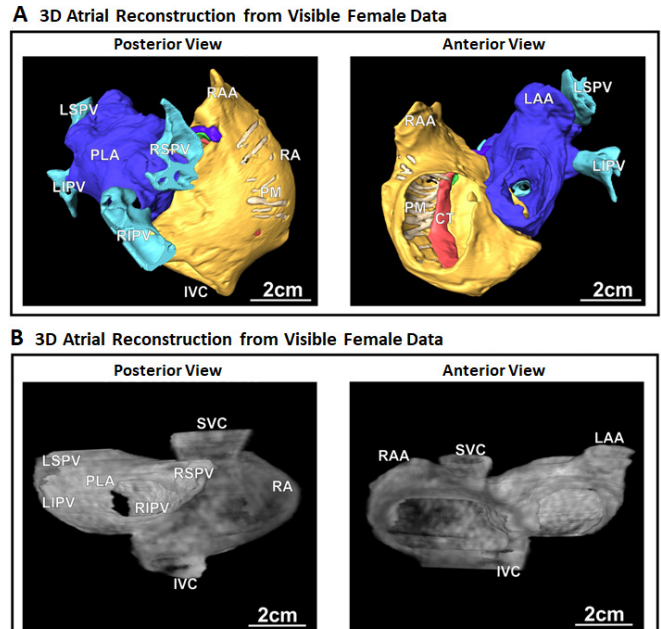


Fig. 2. The 3D human atria used in this study. A) The posterior and anterior view of the *ex vivo* post-mortem 3D human atria. Distinguished atrial anatomical regions are highlighted in different colors. B) The posterior and anterior views of the *in vivo* 3D atria #1 from the LGE-MRI of a patient with AF. Here AF, Atrial fibrillation; LGE-MRI, Late gadolinium-enhanced MRI; CT, crista terminalis; IVC/SVC, inferior/superior vena cava; LA/RA, left/right atrium; LAA/RAA, left/right atrial appendage; LS/LI/RS/RI PV, left superior/left inferior/right superior/right inferior pulmonary vein; PLA, posterior left atrium; PMS, pectinate muscles.

### B. Atrial Epicardial and Endocardial Surface Extraction

Based on the segmented atrial anatomy, the separation of the epicardial and endocardial surfaces from the atrial wall was required to define boundary conditions for solving the Laplace equation [9]. We have developed a convex hull algorithm to obtain the two surfaces. The convex hull in this context was defined as the smallest convex volume that contained all the atrial wall tissue (Fig. 3). The algorithm is an adaptation of the quickhull method [28], which uses the divide and conquer approach. The convex hull approach was initialized by choosing two points of the atrial wall, the maximum and

minimum values of  $x$  coordinates, based on the principle that these extreme points were always a part of the convex hull. The two points were then connected by a straight line which partitioned the atrial wall into two sets. A point on the atrial tissue with the maximum Euclidean distance from the partitioning line in one set was then added to the convex hull to form a triangle, introducing two additional lines. The furthest points from each of the two new lines were subsequently added, repeating the progress recursively until the entire atrial wall was inside the convex hull within one partitioned set. This procedure was repeated for the other partitioned set until the atria was completely enclosed by the resultant convex hull.

Although the convex hull could be calculated directly in 3D, the resultant 3D convex hull would be severely overestimated. It may lead to the connected non-tissue regions (gray) even outside the atria (**Fig. 3B**). Hence, calculating the convex hull slice-by-slice in each 2D plane and then combining all 2D results to form a 3D convex hull would produce a smaller convex hull containing the 3D atria than that generated using a 3D convex hull. Furthermore, we have taken the intersection of the three individual convex hulls computed separately along each of the three imaging planes  $XY$ ,  $YZ$  and  $XZ$ , minimizing the non-tissue volume (gray) captured outside the atrial wall (**Fig. 3C**). A 2D connectivity filter was then applied on each  $XY$  plane to remove overflows of the convex hull (gray) outside the atrial chambers. The atrial epicardial surface was identified by separating the outer atrial surface using the final 3D convex hull (**Fig. 3D**) and a region growing method was used to obtain both the LA and RA cavity. Finally, the LA/RA endocardial surface was obtained by separating the surface of the atrial cavity (**Fig. 3D & 4A**).

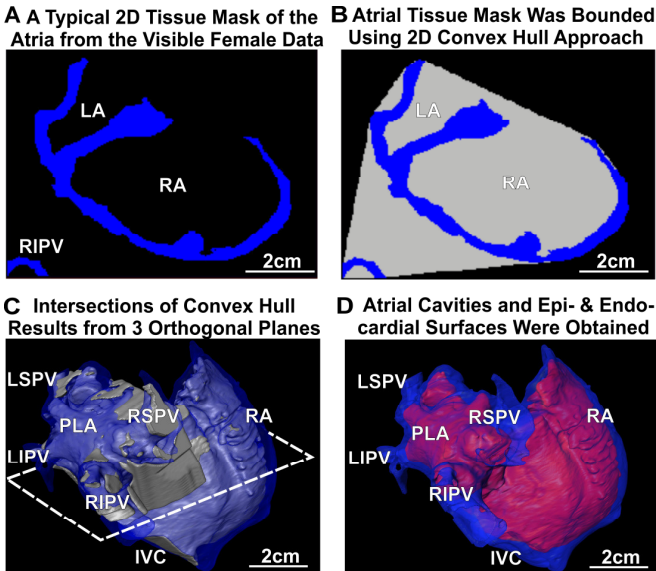


**Fig. 3.** Separation of the epicardial and endocardial surfaces using the convex hull of the 3D human atria. The *ex vivo* data was used for illustration. **A)** A 2D section of the tissue mask (blue) for the atrial wall. **B)** The convex hull (gray) obtained from the 2D tissue mask. **C)** Intersection of the 2D individual convex hulls along the three orthogonal planes. **D)** The reconstruction of the epicardial (blue) and endocardial (red) surfaces obtained using a region growing method based on the final convex hull. For abbreviations, see Fig. 2.

### C. Automatic Atrial Chamber Separation

Separation of the bi-atrial chambers into LA and RA was a crucial step in simplifying 3D AWT estimations since the bi-atrial anatomy was complex. Computing the wall thicknesses for the LA and the RA separately produced more accurate estimates. Here we propose a robust method based on the Laplace equation to automatically define the separating boundary surface between the LA and the RA in 3D.

The Laplace equation is a second-order PDE:

$$\frac{\partial^2 \phi}{\partial x^2} + \frac{\partial^2 \phi}{\partial y^2} + \frac{\partial^2 \phi}{\partial z^2} = 0, \quad (1)$$

where  $\phi(x, y, z)$  is a function of the independent variables  $x$ ,  $y$  and  $z$ . The solutions of the Laplace equation can be estimated numerically by using e.g. the central difference scheme [29]. Concerning the  $x$  variable, this can be written as

$$\frac{\partial^2 \phi}{\partial x^2} \Big|_i = \frac{\phi_{i+1,j,k} - 2\phi_{i,j,k} + \phi_{i-1,j,k}}{h^2}, \quad (2)$$

where  $(i, j, k)$  are the indices of a point along the *coordinate* directions  $x$ ,  $y$ , and  $z$ , and  $\phi_i$ ,  $\phi_{i-1}$  and  $\phi_{i+1}$  indicate function values at different points with a constant distance  $h$  apart along the  $x$ -direction. By substituting the approximation in **Equation 2** for  $y$  and  $z$ , and assuming  $h = 1$  for simplicity, **Equation 1** is rearranged as

$$\phi_{i,j,k} = \frac{\phi_{i+1,j,k} + \phi_{i-1,j,k} + \phi_{i,j,k+1} + \phi_{i,j,k-1}}{6} \quad (3)$$

The successive over-relaxation method [29] was used to numerically solve the discrete Laplace **Equation 3** by linearly combining the new solution with the solution obtained from the previous iteration such that

$$\phi_{i,j,k}^{iteration} = (1 - \omega)\phi_{i,j,k}^{iteration-1} + \omega\phi_{i,j,k} \quad (4)$$

with a relative error for each point of

$$\epsilon_{i,j,k} = \left| \frac{\phi_{i,j,k}^{iteration-1} - \phi_{i,j,k}^{iteration}}{\phi_{i,j,k}^{iteration-1}} \right|. \quad (5)$$

The most common relaxation factor  $\omega = 1.4$  was used [29]. A Dirichlet boundary condition was imposed to produce a unique solution to **Equation 3** with different values at the surfaces. In our study, we set 300 at the LA endocardium and 100 at the RA endocardium, and 200 for the bi-atrial epicardial surface (**Fig. 4B**). This resulted in the Laplacian solution between 100 and 300 within the atrial wall, and the value of 200 in the solution space could be used to determine the boundary for separating the LA and the RA (**Fig. 4C**). Hence the LA was the region where the values of the Laplace solutions were  $>200$  and the RA was the region where the values were  $\leq 200$  (**Fig. 4D**).

### D. Atrial Wall Thickness Estimation

Many approaches currently exist for calculating 3D wall thickness. Three of the most widely used methods: the nearest distance, the surface normal and Laplace solution, are briefly outlined in this sub-section, followed by our proposed coupled PDEs approach for calculating the 3D AWT.

**The Nearest Distance** – The nearest distance method was the simplest and most intuitive approach for estimating the wall

thickness. For the 3D atrial wall, the thickness was estimated by determining the shortest distance from a point of interest on a reference surface, e.g., the endocardial surface, to an opposite surface of interest, e.g., the epicardial surface. This often led to inaccurate measurement where atrial anatomy was complex with large variation in the thickness.

**The Surface Normal** – The surface normal method was another simple approach for estimating the AWT by using vectors normal to a surface. Given the endocardial surface, a line perpendicular to a reference point on the surface was constructed from the local tangent plane. The line could then be extended to the epicardial surface, and the thickness was determined as the length of the resultant line segment that lay between the epicardial and endocardial surfaces. This method was effective in most regions of the atrial wall but failed to produce accurate measurement at areas with drastic changes in the tissue thickness or shape.

**The Laplace Solution** – The Laplace solution for estimating the AWT (**Equation 3 & Fig. 4B**) used the Laplace solution as described in the previous sub-section to generate the gradient vector field throughout the walls [9]. Trajectories were then traced from the point of interest on the endocardial surface along the direction of the gradient field to the epicardium. The AWT was then approximated by the length of the trajectories. Compared with the two aforementioned methods, this approach was more robust as it accounted for the variation in geometry throughout the atrial walls.

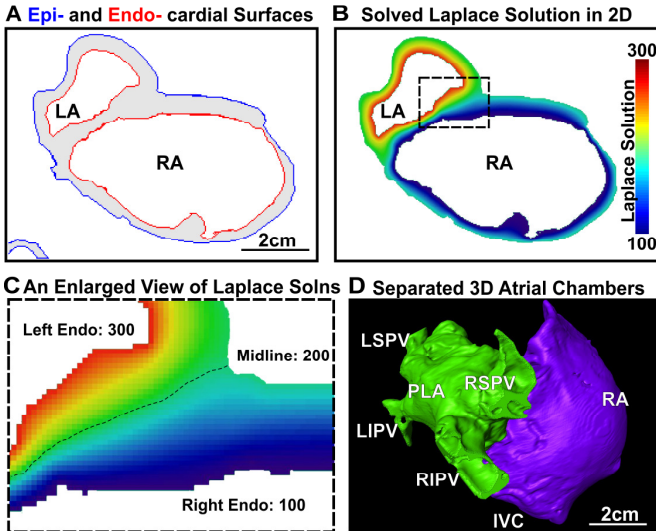


**Fig. 4.** The automatic separation of the LA and RA chambers by solving the Laplace equation. **A)** The epicardial (blue) and endocardial (red) surfaces of the atria were highlighted in 2D. **B)** Numerically obtained Laplace solution with fixed values at epicardial (200) and endocardial (300 for RA and 100 for LA) surfaces. The dashed rectangular box region is enlarged and displayed in **C)**. The dashed line separated the RA and LA where the Laplace solution equaled 200 (the mid-value). **D)** The resultant LA and RA chambers were reconstructed in 3D. For abbreviations, see Fig 2.

**The Coupled PDEs** – The proposed PDE method yielded the most accurate AWT estimates and was more robust than the methods above. It used the Laplace solution (**Equation 3**) but differed from the previous approach as in addition, two first-order linear PDEs were solved to calculate wall thickness between the atrial surfaces instead of explicitly calculating the trajectories from the gradient field. Here, we describe how the

couple PDEs are derived, as well as a numerical approach for solving these.

The normalized gradient field,  $T$ , of the Laplace solution  $\phi$  is

$$T = \frac{\nabla\phi}{\|\nabla\phi\|} \quad (6)$$

where  $\nabla$  is the gradient function. According to co-ordinate geometry and the definition of  $T$ , the trajectory functions must satisfy the first-order linear PDEs

$$\nabla D_{epi} \cdot T = 1, \quad \text{with } D_{epi}|_{\Gamma_{epi}} = 0 \quad (7)$$

$$-\nabla D_{endo} \cdot T = 1, \quad \text{with } D_{endo}|_{\Gamma_{endo}} = 0 \quad (8)$$

where  $D_{epi}(l)$  is the trajectory function of the distance from the epicardial surface  $\Gamma_{epi}$ , and  $D_{endo}(l)$  is the trajectory function of the distance from the endocardial surface  $\Gamma_{endo}$ . The AWT can therefore be obtained by combining the two trajectory functions such that

$$\text{Thickness}(x) = D_{epi}(l) + D_{endo}(l). \quad (9)$$

Solving the coupled PDE **Equations 1, 7, and 8** numerically is not straightforward. The Laplace solution was first obtained as described in the previous sub-section IIC and an upwind scheme was used to discretize the two first-order linear PDEs (**Equation 7 and 8**) [30]. By assuming  $\nabla\phi$  is a unit vector, **Equation 7** can be expanded into

$$\frac{\partial\phi}{\partial x} \frac{\partial D_{epi}}{\partial x} + \frac{\partial\phi}{\partial y} \frac{\partial D_{epi}}{\partial y} + \frac{\partial\phi}{\partial z} \frac{\partial D_{epi}}{\partial z} = 1. \quad (10)$$

At each grid point  $(x_i, y_j, z_k)$ , the partial derivative of the distance function was approximated differently depending on the direction of the gradient field. By following the first-order upwind scheme, conditional terms were introduced such that **Equation 10** becomes

$$\frac{\partial\phi}{\partial x} \left\{ \begin{array}{l} \frac{D_{epi}(i,j,k) - D_{epi}(i-1,j,k)}{h_x}, \quad \text{if } \frac{\partial\phi}{\partial x} > 0 \\ \frac{D_{epi}(i+1,j,k) - D_{epi}(i,j,k)}{h_x}, \quad \text{otherwise} \end{array} \right\} + \frac{\partial\phi}{\partial y} \left\{ \begin{array}{l} \frac{D_{epi}(i,j,k) - D_{epi}(i,j-1,k)}{h_y}, \quad \text{if } \frac{\partial\phi}{\partial y} > 0 \\ \frac{D_{epi}(i,j+1,k) - D_{epi}(i,j,k)}{h_y}, \quad \text{otherwise} \end{array} \right\} + \frac{\partial\phi}{\partial z} \left\{ \begin{array}{l} \frac{D_{epi}(i,j,k) - D_{epi}(i,j,k-1)}{h_z}, \quad \text{if } \frac{\partial\phi}{\partial z} > 0 \\ \frac{D_{epi}(i,j,k+1) - D_{epi}(i,j,k)}{h_z}, \quad \text{otherwise} \end{array} \right\} = 1 \quad (11)$$

Note the characteristics of the first-order PDEs are exactly the correspondence trajectories which never intersect. Therefore, we do not need to worry about shocks, in contrast to many first-order boundary value PDEs. Due to this, we do not need to be concerned with entropy conditions in the numerical schemes to solve these PDEs. The upwind conditioning scheme is necessary here [30]. Assuming that  $h_x = h_y = h_z = 1$ , **Equation 11** can be simplified and re-arranged to formulate the trajectory function of the distance from the epicardial surface:

$$D_{epi}(i,j,k) = \frac{1 + \frac{\partial u}{\partial x} D_{epi}(i\mp 1,j,k) + \frac{\partial u}{\partial y} D_{epi}(i,j\mp 1,k) + \frac{\partial u}{\partial z} D_{epi}(i,j,k\mp 1)}{\frac{\partial\phi}{\partial x} + \frac{\partial\phi}{\partial y} + \frac{\partial\phi}{\partial z}}$$

$$\text{where } \mp 1 = \begin{cases} i-1, & \frac{\partial\phi}{\partial x} > 0 \\ i+1, & \frac{\partial\phi}{\partial x} < 0 \end{cases}, \quad j\mp 1 = \begin{cases} j-1, & \frac{\partial\phi}{\partial y} > 0 \\ j+1, & \frac{\partial\phi}{\partial y} < 0 \end{cases}, \quad \text{and}$$

$$k \mp 1 = \begin{cases} k - 1, & \frac{\partial \phi}{\partial z} > 0 \\ k + 1, & \frac{\partial \phi}{\partial z} < 0 \end{cases}. \quad (12)$$

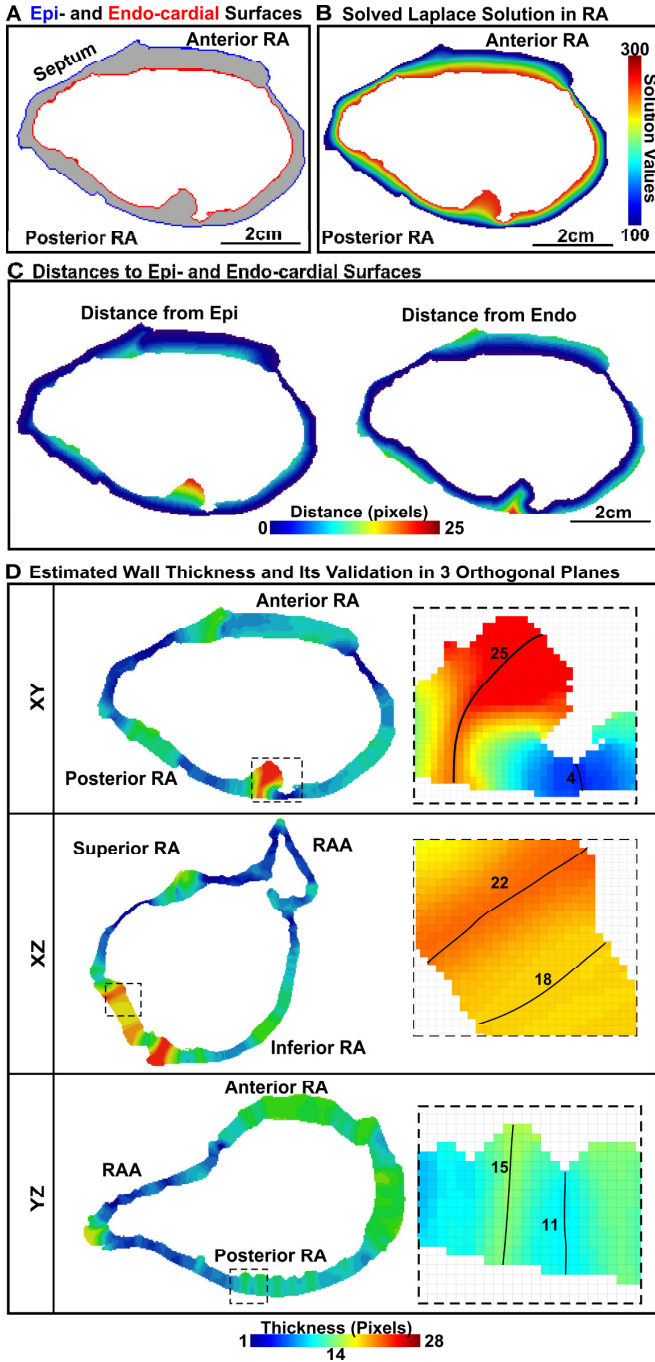


**Fig. 5.** The coupled PDEs method to calculate the atrial wall thickness and its validation on the *ex vivo* data. **A)** Epicardial (blue) and endocardial (red) surfaces obtained by using the convex hull approach. **B)** Laplace solutions for the RA solved with fixed boundary values (300 for endocardium and 100 for epicardium). **C)** The distances calculated using the two trajectory functions by solving coupled PDEs. **D)** The estimated wall thickness calculated by the coupled PDE approach displayed in the three orthogonal planes and validated by comparing with the manually measured values (solid black line).

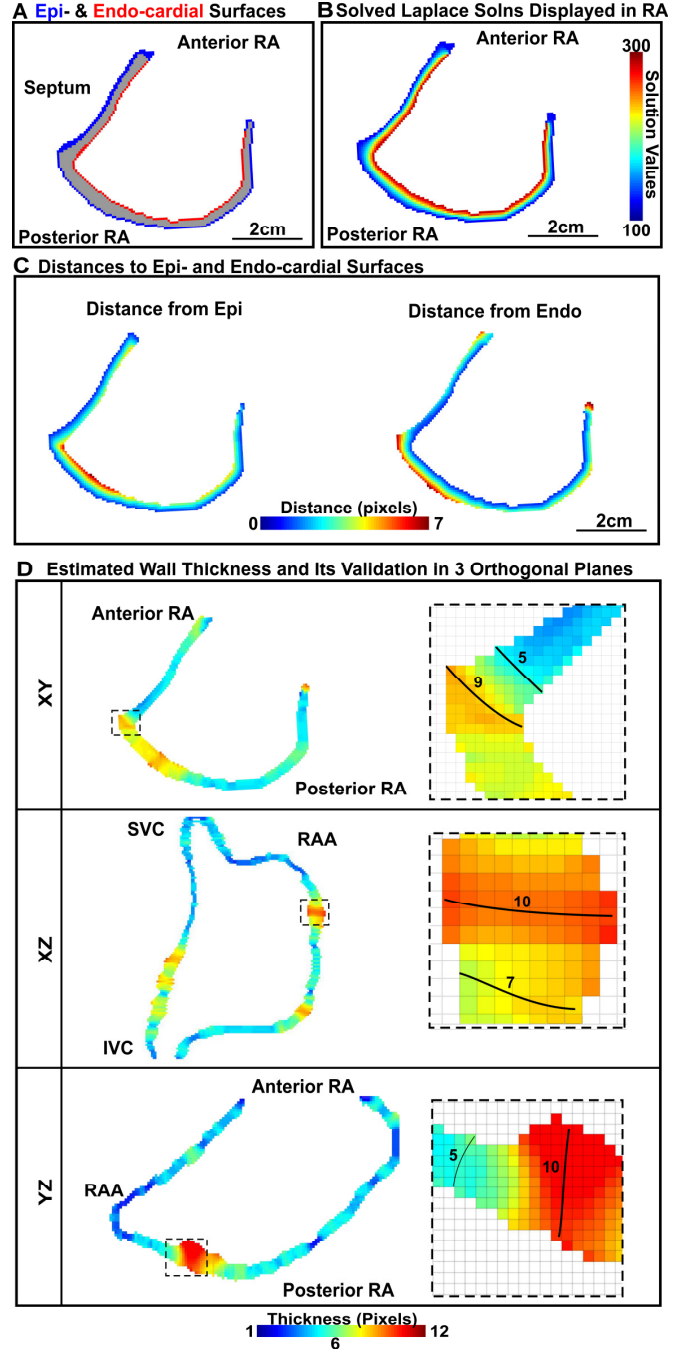


**Fig. 6.** The coupled PDEs method to calculate the atrial wall thickness and its validation on the *in vivo* data #1. **A)** Epicardial (blue) and endocardial (red) surfaces obtained by using the convex hull approach. **B)** Laplace solutions for the RA solved with fixed boundary values (300 for endocardium and 100 for epicardium). **C)** The distances calculated by the two trajectory functions. **D)** The estimated wall thickness calculated by the coupled PDE approach displayed in the three orthogonal planes and validated by comparing with the manually measured values (solid black line).

Similarly, the trajectory function of the distance from the endocardial surface,  $D_{endo}(l)$ , can be substituted through **Equations 10** and **11** such that **Equation 8** becomes

$$D_{endo(i,j,k)} = \frac{1 + \frac{\partial u}{\partial x} D_{endo(i \pm 1, j, k)} + \frac{\partial u}{\partial y} D_{endo(i, j \pm 1, k)} + \frac{\partial u}{\partial z} D_{endo(i, j, k \pm 1)}}{\frac{\partial \phi}{\partial x} + \frac{\partial \phi}{\partial y} + \frac{\partial \phi}{\partial z}}$$

$$\text{where } i \pm 1 = \begin{cases} i + 1, & \frac{\partial \phi}{\partial x} > 0 \\ i - 1, & \frac{\partial \phi}{\partial x} < 0 \end{cases}, \quad j \pm 1 = \begin{cases} j + 1, & \frac{\partial \phi}{\partial y} > 0 \\ j - 1, & \frac{\partial \phi}{\partial y} < 0 \end{cases}, \quad \text{and} \\ k \pm 1 = \begin{cases} k + 1, & \frac{\partial \phi}{\partial z} > 0 \\ k - 1, & \frac{\partial \phi}{\partial z} < 0 \end{cases}. \quad (13)$$

The discrete schemes (Equations 12 and 13) were solved numerically and the two trajectory functions from the epicardial and endocardial surfaces were obtained for all grid points inside the atrial wall (Fig. 5C and 6C). The solutions of trajectory functions  $D_{epi}(l)$  and  $D_{endo}(l)$  smoothly increased from 0 to 8.25 mm towards the opposite surface, and the sum of the two yielded the 3D AWT map for each atrial chamber (left panel in Fig. 5D and 6D).

### III. RESULTS

We first validated the AWT estimation from the proposed automatic algorithms by comparing with manually identified ground truth measurements. The *ex vivo* human atria and the *in vivo* data were used to demonstrate the accuracy of our proposed method, as well as to visualize the distribution of the wall thicknesses across the atrial walls. Finally, the AWT summary statistics for the three data are shown and analyzed.

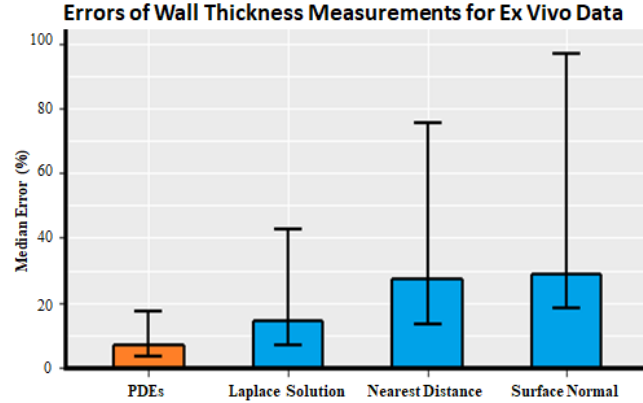


Fig. 7. The relative errors for atrial wall thickness estimation using different algorithms compared to the manual measurements on the *ex vivo* human atria data. The bar represents the median and errors represent the 1<sup>st</sup>/3<sup>rd</sup> quantiles.

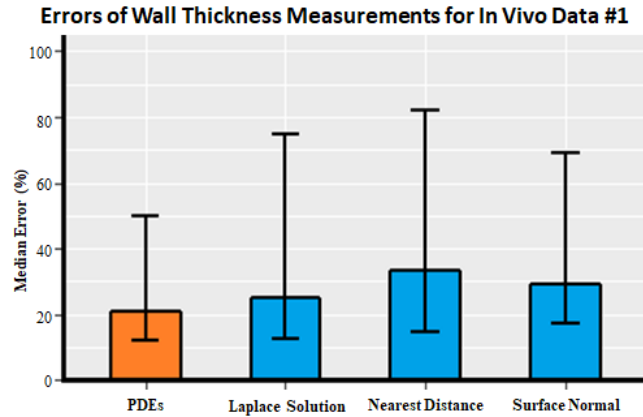


Fig. 8. The relative errors for atrial wall thickness estimation using different algorithms compared to the manual measurements on the *in vivo* human atria #1. The bar represents the median and errors represent the 1<sup>st</sup>/3<sup>rd</sup> quantiles.

#### A. Validation of Wall Thickness Estimation

To validate the AWT calculations from the automated methods aforementioned, the ground truth measurements at multiple locations along the atrial wall were obtained by an independent researcher, blind to the automatic approaches and results, manually counting the number of pixels in the region that defined the thickness and multiplying the count by the spatial resolution. These AWT values were then compared with the results obtained from the automated methods at the same locations, and the errors were evaluated. Examples of manual AWT calculations are shown on the right-side panel in Fig. 5D & 6D, with the 50 points chosen for evaluation shown in Fig. S1. The average of the relative errors of the proposed algorithms along the 3D atrial wall of *ex vivo* human atria and *in vivo* data #1 are shown in Fig. 7 & 8. The proposed coupled PDEs approach was the most accurate with a relative error of 8% for the *ex vivo* data and 21% for the *in vivo* data and significantly outperformed the other algorithms. The nearest distance method was the least accurate with an average error of 34% for both human atria data while the Laplace solution methods had error rates of 15% for the *ex vivo* data and 25% for the *in vivo* data (Fig. 7).

#### B. Comparison of Wall Thickness Estimation Algorithms

The 3D AWT maps generated from the four different algorithms are shown in Fig. 9 & 10 for the *ex vivo* data and *in vivo* data #1 respectively and in Fig. S2 for the *in vivo* data #2. The red color key indicates thick atrial tissue while the blue regions indicate thin atrial tissue. Since the coupled PDEs approach was shown to be accurate within 8% of the ground truth, the 3D maps produced from this approach (Fig. 9D & 10D) can be an indication of the true AWT distribution of the patient data, and was used to compare the efficacy of the other approaches. Compared to the ground truth measurements, the nearest neighbor method tended to underestimate the wall thickness, while the surface normal and the Laplace solution methods tended to overestimate the wall thickness. It can be seen from Fig. 9 that all four AWT estimation approaches resulted in a higher AWT value around the crista terminalis (CT). The nearest neighbor approach (Fig. 9A) heavily underestimated the AWT around the CT area and other areas with larger wall thicknesses. The overestimation by the surface normal approach (Fig. 9B) could be seen by the high AWT values in areas of complex geometry such as the posterior left atrial wall and around the CT and pectinate muscles. The Laplace solution approach (Fig. 9C) was observed to overestimate the AWT around the CT, and posterior left atrial region, but captured the AWT variation patterns similar to that of the coupled PDEs approach (Fig. 9D). Similar AWT patterns could be observed from the *in vivo* human atria #1 where the nearest neighbor approach (Fig. 10A) slightly underestimated the wall thickness, and the surface normal approach and Laplace solution approach (Fig. 10B&C) heavily overestimated the AWT in the right atrium close to the septum area with high variation in wall thickness. Overall, the four methods captured similar characteristics about the AWT distribution across the atrial walls; however, the actual thickness values computed differed significantly. Comparisons of the difference in 3D AWT distributions computed by each

method are shown in the Supplemental **Fig. S3** and **Table S1**. As we can see the difference between Laplace and coupled PDE approaches is quite small, except the regions in distal pulmonary veins.

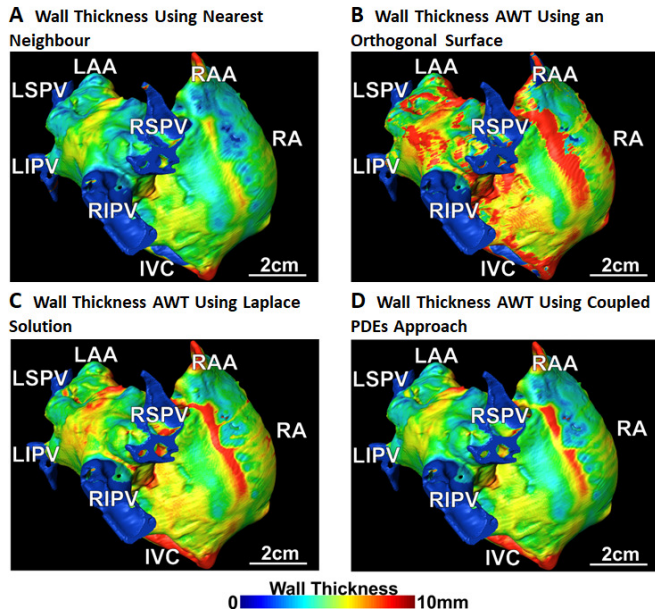


**Fig. 9.** The 3D atrial wall thickness was visualized on the *ex vivo* human atria using different algorithms. The coupled PDE approach yielded the most accurate estimation.

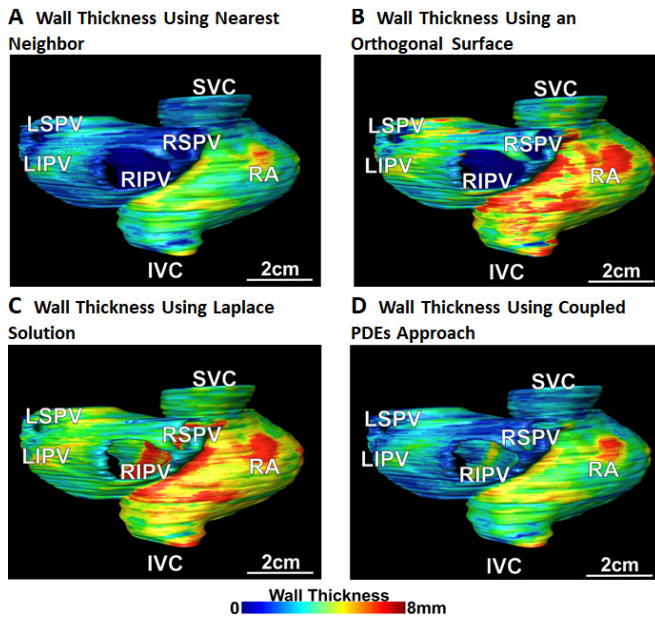


**Fig. 10.** The 3D atrial wall thickness was visualized on the *in vivo* human atria #1 using different algorithms. The coupled PDE approach yielded the most accurate estimation.

### C. Atrial Wall Thickness

The summary statistics of the wall thicknesses of the three human atria (1 *ex vivo* and 2 *in vivo* hearts) using the coupled PDE approach are shown in **Fig. 11**, and the other three methods in **Fig. S4**. Overall, the median thickness was approximately 2.5 mm for the RA and 1.9 mm for the LA. For all three patients, the RA wall was on average 0.7 mm thicker

than the LA wall. While the maximum thickness of the RA wall was significantly higher than the maximum thickness of the LA wall, the minimum thicknesses for both were approximately the same across all patients (~0.7 mm). The average wall thicknesses for the three patients were consistent for the LA and RA; however, there were large variations among human hearts in the maximum thicknesses for the RA (6.7 mm to 10.0 mm) and LA (4.5 mm to 8.9mm) walls. It could also be seen that there was a slightly greater variation of thickness in the RA wall (standard deviation of 1.3 mm) compared to the LA wall (standard deviation of 1.0 mm). The maximum AWT measurements in the *ex vivo* patient data for both atria were significantly higher than the two *in vivo* patient data, which were fairly consistent.

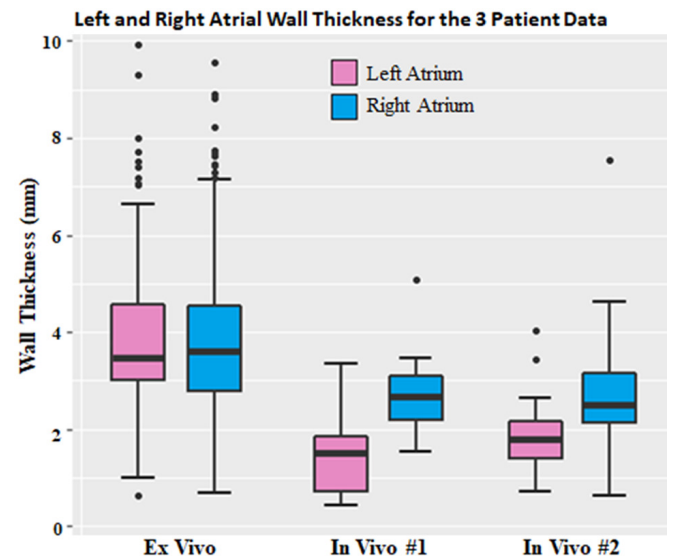


**Fig. 11.** A box plot of the wall thicknesses for the three human hearts used in this study, grouped by the left and right atrial walls.

## IV. DISCUSSION

AF is the most common sustained heart rhythm disturbance and is associated with substantial morbidity and mortality. It has been known that AF is driven by complex substrates which are distributed widely throughout both atrial chambers [31], and the atrial structure plays an important role in physiological and pathophysiological conditions [32, 33]. AWT variation is demonstrated to have an important role in AF arrhythmogenesis and has an influence on activation patterns during arrhythmias due to source-sink relationship in the conduction of the activation waves [34, 35]. Furthermore, AWT is a very important factor that is required to select an appropriate radiofrequency energy level in order to achieve safe and reliable transmural lesions during a clinical ablation procedure [36]. To the best of our knowledge, for the first time, we have developed and validated a robust computational framework for the calculation of 3D bi-atrial wall thickness distribution.

### A. Automatic Epicardial and Endocardial Surface Extraction

The complex structure of the bi-atrial chambers makes the automatic separation of epicardial and endocardial surfaces, which define the boundaries that enclose the atrial wall

difficult. This is mainly due to multiple openings in its 3D structure such as the four pulmonary veins and mitral valve of the LA and the tricuspid valve of the RA. A region growing approach was developed in a study of the ventricular structure by Golds and Beg [37] to detect the endocardium surface, which was then subtracted from the continuous ventricle wall surface to obtain the epicardium surface. However, due to the multi-openings of the atrial anatomy, this approach is not feasible. Manually closing the openings of the atria before the application of a region growing method is also feasible, but is labor intensive and prone to bias. The efficiency of our framework lies in the automatic separation of the epicardial and endocardial surfaces using a novel implementation of a convex hull based method. This allows the entire pipeline to be completely automated from the raw 3D atrial anatomy to the 3D AWT map. Furthermore, the separation of the LA and RA chambers using the Laplace solution is effective in our study for robust AWT estimation.

### B. Automatic Wall Thickness Estimation

In the past, many approaches have been proposed to estimate the tissue thickness, but these results vary greatly due to the nature of these methods utilized across different studies [6-9, 18, 22, 38]. The nearest neighbor approach is simple and efficient to implement and has shown promising results when it was used to estimate cortical thickness in the brain [39]. However, when this method was applied for the human atria, the AWT estimation was significantly underestimated compared with the ground truth measurement. Similarly, the surface normal approach is also intuitive to implement but is error-prone in areas where there are large geometrical variations in the AWT [16-18]. Results of wall thickness using the surface normal approach are also dependent on the reference surface, i.e., the endocardial surface or epicardial surface. This is because this method only considers one boundary condition when formulating the normal vectors spanning across the atrial wall and ignoring the opposite boundary. The Laplace solution approach is a more robust approach for tissue thickness estimation as it considers the varying geometry of both tissue surfaces. The accuracy of the Laplace solution approach has been proven in many cortical and ventricular wall thickness studies [9, 40] but it requires a time-consuming streamline tracing approach to calculate the tissue thickness from the gradient field of the resultant Laplace solutions. Furthermore, the results from our numerical experiments on the atrial wall show that this approach tends to overestimate AWT similarly to the surface normal method.

The most recent benchmarking study for LA segmentation and thickness comprehensively explored three algorithms for CT and MRI image database respectively and validated on ten 3D subjects each [8]. However, the thickness was determined as the shortest Euclidean distance from the outer to the inner boundary of the atrial wall, which leads to spurious lengths in some regions. In our proposed framework, a coupled PDEs method was used to estimate the bi-atrial chamber wall thickness. Of all the approaches tested in this study, the coupled PDEs approach produced the most accurate AWT estimate when validated against manual measurements. Its superior accuracy can be attributed to the fact that the coupled PDE

method implicitly solves the distant trajectories mapping the epicardial and endocardial surfaces instead of explicitly defining them as in other methods. The formulation of the coupled PDEs by incorporating the Laplace equation also increases its effectiveness as the varying geometries of both epicardial and endocardial surfaces are integrated into the system. This leads to a more realistic representation of the AWT at each solution grid along the atrial wall. Our numerical results show the superior accuracy across the entire bi-atrial chambers, especially where other methods perform poorly due to a sudden change in regional wall thickness.

### C. Human Atrial Wall Thickness

In the past, human AWT estimated using various approaches was reported widely for LA due to its importance in AF. In a study of 26 explanted human hearts by manual measurement, Ho et al. [38] reported a range of 1.5 mm to 4.8 mm for the LA anterior wall and Sánchez-Quintana et al. [41] reported a range of 2.8 mm to 12 mm at the inferior-posterior wall, centrally between the junction of LA and the left/right pulmonary vein. In the first computer model of human atria, Harrild and Henriquez [42] modeled the LA wall thickness varying from 0.3 to 4.1 mm. In our recent study of explanted human atria [6] imaged using high-resolution contrast-enhanced MRIs, we reported the LA wall with a median value of 3.4 mm varying from 1.1 to 8.6 mm. Unlike *ex vivo* AWT, *in vivo* AWT values are difficult to measure and validate directly. In contrast, LA wall thickness reported relatively lower values from the studies of human atria *in vivo*. For an example, Karim et al. [8] reported  $1.16 \pm 0.88$  mm in the anterior section of LA wall and  $1.23 \pm 1.10$  mm for posterior LA by averaging over all ten human atria.

The discrepancy in human AWT between *ex vivo* and *in vivo* hearts is observed in RA as well. In our contrast-enhanced MRI study of explanted human atria [6], we reported the RA AWT with a median value of 3.8 mm varying from 0.4 to 11.7 mm. Ginami et al. have developed the approach of black-blood quantification for estimating AWT and reported  $2.54 \pm 0.87$  mm for RA in 11 healthy subjects.

Most of the studies above are based on one atrial chamber only. In this study, our AWT estimation results in a range from 0.7 to 9.9 mm in bi-atrial chambers, which is consistent with the direct measurement on the *ex vivo* studies. Interestingly, we also found the wall thickness values measured from human atria *in vivo* are consistently lower than the values measured in *ex vivo* studies. This difference is possibly due to the limitations in the spatial resolution of different imaging modalities. Overall, the AWTs estimated from our framework coincide with those presented in existing literature, validating its potential to provide accurate 3D atrial analysis.

### D. Limitations

Like any study, this study has several limitations. Firstly, during the division of the atrial septum to separate the LA and RA chambers, assumptions had to be made for the splitting ratio. In this study, the septum was divided evenly between the LA and RA. Anatomically, this may not be the case as the sizes of the LA and RA differ slightly. If the interatrial septal thickness is needed, additional post-processing will be needed to stitch the LA and RA septum into one component. Secondly,

our estimated errors among the benchmarked approaches are limited due to only a small number of locations used for comparisons. Ideally, an atrial phantom is needed to comprehensively validate AWT across the atrial chambers. However, our calculated errors are consistent across different data for each evaluated approach, which may indicate the selected locations to be representative. Finally, our utilized image data size ( $n=3$ ) is small. The focus of this study is to explain and validate our method in detail. In the near future, we will conduct another large scale study to include more human hearts both in vivo and ex vivo for clinical insights, as well as extensive comparisons with other existing wall distance methods [43,44].

Although the proposed approach is robust, we have to be aware that AWT varies from 0.4 to 11.7 mm. Therefore, it will lead to inherited errors due to the low resolution of image data. A robust finite element mesh approach may be a better representation of atrial surfaces and lead to further improvements in the AWT estimate for the proposed PDE approach.

## V. CONCLUSION

In this study, we have developed and evaluated a robust computational framework for automatically measuring the AWT from clinically obtained medical images. Multiple algorithms were introduced in the framework which resulted in the elimination of all manual processes used in previous studies. Our framework enables the reconstruction and visualization of the 3D wall thickness for the bi-atrial chambers with a relative error of 8%, and outperforms existing algorithms by over 7%. The methods proposed in our study can potentially be used to improved clinical diagnosis, patient stratification, and clinical guidance during ablation treatment for patients with abnormal heart rhythms.

## REFERENCES

- [1] M. Zoni-Berisso, F. Lercari, T. Carazza, and S. Domenicucci, "Epidemiology of atrial fibrillation: European perspective," *Clinical epidemiology*, vol. 6, p. 213, 2014.
- [2] P. A. Barber, R. Krishnamurthi, V. Parag, N. E. Anderson, A. Ranta, D. Kilfoyle, *et al.*, "Incidence of transient ischemic attack in Auckland, New Zealand, in 2011 to 2012," *Stroke*, vol. 47, pp. 2183-2188, 2016.
- [3] S. M. Narayan and J. A. B. Zaman, "Mechanistically-based mapping of human cardiac fibrillation," *The Journal of Physiology*, vol. 594, pp. 2399-2415, 2016.
- [4] G. Lee, S. Kumar, A. Teh, A. Madry, S. Spence, M. Larobina, *et al.*, "Epicardial wave mapping in human long-lasting persistent atrial fibrillation: Transient rotational circuits, complex wavefronts, and disorganized activity," *European Heart Journal*, vol. 35, pp. 86-97, 2014.
- [5] M. Haissaguerre, A. J. Shah, H. Cochet, M. Hocini, R. Dubois, I. Efimov, *et al.*, "Intermittent drivers anchoring to structural heterogeneities as a major pathophysiologic mechanism of human persistent atrial fibrillation," *The Journal of physiology*, 2016.
- [6] J. Zhao, B. J. Hansen, Y. Wang, T. A. Csepe, L. V. Sul, A. Tang, *et al.*, "Three-dimensional Integrated Functional, Structural, and Computational Mapping to Define the Structural "Fingerprints" of Heart-Specific Atrial Fibrillation Drivers in Human Heart Ex Vivo," *Journal of the American Heart Association*, vol. 6, p. e005922, 2017.
- [7] B. J. Hansen, J. Zhao, T. A. Csepe, B. T. Moore, N. Li, L. A. Jayne, *et al.*, "Atrial fibrillation driven by micro-anatomic intramural re-entry revealed by simultaneous sub-epicardial and sub-endocardial optical mapping in explanted human hearts," *European heart journal*, vol. 36, pp. 2390-2401, 2015.
- [8] R. Karim, L.-E. Blake, J. Inoue, Q. Tao, S. Jia, R. J. Housden, *et al.*, "Algorithms for left atrial wall segmentation and thickness-Evaluation on an open-source CT and MRI image database," *Medical image analysis*, vol. 50, pp. 36-53, 2018.
- [9] M. Bishop, R. Rajani, G. Plank, N. Gaddum, G. Carr-White, M. Wright, *et al.*, "Three-dimensional atrial wall thickness maps to inform catheter ablation procedures for atrial fibrillation," *Europace*, vol. 18, pp. 376-383, 2015.
- [10] J.-S. Song, J. Wi, H.-J. Lee, M. Hwang, B. Lim, T.-H. Kim, *et al.*, "Role of atrial wall thickness in wave-dynamics of atrial fibrillation," *PLoS one*, vol. 12, p. e0182174, 2017.
- [11] A. Roy, M. Varela, and O. Aslanidi, "Image-Based Computational Evaluation of the Effects of Atrial Wall Thickness and Fibrosis on Re-entrant Drivers for Atrial Fibrillation," *Frontiers in Physiology*, vol. 9, 2018.
- [12] R. Andlauer, G. Seemann, L. Baron, O. Dössel, P. Kohl, P. Platonov, *et al.*, "Influence of left atrial size on P-wave morphology: differential effects of dilation and hypertrophy," *EP Europace*, vol. 20, pp. iii36-iii44, 2018.
- [13] R. S. Oakes, T. J. Badger, E. G. Kholmovski, N. Akoum, N. S. Burgon, E. N. Fish, *et al.*, "Detection and quantification of left atrial structural remodeling with delayed-enhancement magnetic resonance imaging in patients with atrial fibrillation," *Circulation*, vol. 119, pp. 1758-1767, 2009.
- [14] K. Higuchi, J. Cates, G. Gardner, A. Morris, N. S. Burgon, N. Akoum, *et al.*, "The Spatial Distribution of Late Gadolinium Enhancement of Left Atrial MRI in Patients With Atrial Fibrillation," *JACC: Clinical Electrophysiology*, 2017.
- [15] J. Whitaker, R. Rajani, H. Chubb, M. Gabrawi, M. Varela, M. Wright, *et al.*, "The role of myocardial wall thickness in atrial arrhythmogenesis," *EP Europace*, vol. 18, pp. 1758-1772, 2016.
- [16] C. Tobon-Gomez, C. Butakoff, P. Yushkevich, M. Huguet, and A. Frangi, "3D mesh based wall thickness measurement: identification of left ventricular hypertrophy phenotypes," in *Engineering in Medicine and Biology Society (EMBC), 2010 Annual International Conference of the IEEE*, 2010, pp. 2642-2645.
- [17] R. Beyar, E. P. Shapiro, W. L. Graves, W. J. Rogers, W. H. Guier, G. A. Carey, *et al.*, "Quantification and validation of left ventricular wall thickening by a three-dimensional volume element magnetic resonance imaging approach," *Circulation*, vol. 81, pp. 297-307, 1990.
- [18] M. Varela, R. Morgan, A. Theron, D. Dillon-Murphy, H. Chubb, J. Whitaker, *et al.*, "Novel MRI technique enables non-invasive measurement of atrial wall thickness," *IEEE transactions on medical imaging*, vol. 36, pp. 1607-1614, 2017.
- [19] N. Beohar, J. D. Flaherty, C. J. Davidson, M. I. Vidovich, A. Brodsky, D. C. Lee, *et al.*, "Quantitative assessment of regional left ventricular function with cardiac MRI: Three-dimensional centersurface method," *Catheterization and Cardiovascular Interventions*, vol. 69, pp. 721-728, 2007.
- [20] E. Bolson and F. Sheehan, "Centersurface model for 3d analysis of regional left ventricular function," in *Computers in Cardiology 1993, Proceedings.*, 1993, pp. 735-738.
- [21] J. L. Durand, B. Tang, D. E. Gutstein, S. Petkova, M. M. Teixeira, H. B. Tanowitz, *et al.*, "Dyskinesia in Chagasic myocardium: centerline analysis of wall motion using cardiac-gated magnetic resonance images of mice," *Magnetic resonance imaging*, vol. 24, pp. 1051-1057, 2006.
- [22] J.-Y. Sun, C.-H. Yun, G. S. Mok, Y.-H. Liu, C.-L. Hung, T.-H. Wu, *et al.*, "Left Atrium Wall-mapping Application for Wall Thickness Visualisation," *Scientific reports*, vol. 8, p. 4169, 2018.
- [23] G. Ginami, K. López, R. K. Mukherjee, R. Neji, C. Munoz, S. Roujol, *et al.*, "Non-contrast enhanced simultaneous 3D whole-heart bright-blood pulmonary veins visualization and black-blood quantification of atrial wall thickness," *Magnetic resonance in medicine*, vol. 81, pp. 1066-1079, 2019.
- [24] O. Dössel, M. W. Krueger, F. M. Weber, M. Wilhelms, and G. Seemann, "Computational modeling of the human atrial anatomy and electrophysiology," *Medical & Biological Engineering & Computing*, vol. 50, pp. 773-799, 2012.
- [25] G. Seemann, C. Höper, F. B. Sachse, O. Dössel, A. V. Holden, and H. Zhang, "Heterogeneous three-dimensional anatomical and electrophysiological model of human atria," *Philosophical*

- Transactions of the Royal Society of London A: Mathematical, Physical and Engineering Sciences*, vol. 364, pp. 1465-1481, 2006.
- [26] C. McGann, N. Akoum, A. Patel, E. Kholmovski, P. Revelo, K. Damal, *et al.*, "Atrial fibrillation ablation outcome is predicted by left atrial remodeling on MRI," *Circulation: Arrhythmia and Electrophysiology*, p. CIRCEP. 113.000689, 2013.
- [27] Z. Xiong, V. V. Fedorov, X. Fu, E. Cheng, R. Macleod, and J. Zhao, "Fully automatic left atrium segmentation from late gadolinium enhanced magnetic resonance imaging using a dual fully convolutional neural network," *IEEE Transactions on Medical Imaging*, 2018.
- [28] C. B. Barber, D. P. Dobkin, and H. Huhdanpaa, "The quickhull algorithm for convex hulls," *ACM Transactions on Mathematical Software (TOMS)*, vol. 22, pp. 469-483, 1996.
- [29] J. Zhao, M. Davison, and R. M. Corless, "Compact finite difference method for American option pricing," *Journal of Computational and Applied Mathematics*, vol. 206, pp. 306-321, 2007.
- [30] A. J. Yezzi and J. L. Prince, "An Eulerian PDE approach for computing tissue thickness," *IEEE Transactions on Medical Imaging*, vol. 22, pp. 1332-1339, 2003.
- [31] S. M. Narayan, T. Baykaner, P. Clopton, A. Schricker, G. G. Lalani, D. E. Krummen, *et al.*, "Ablation of rotor and focal sources reduces late recurrence of atrial fibrillation compared with trigger ablation alone: extended follow-up of the CONFIRM trial (Conventional Ablation for Atrial Fibrillation With or Without Focal Impulse and Rotor Modulation)," *Journal of the American College of Cardiology*, vol. 63, pp. 1761-1768, 2014.
- [32] J. Zhao, R. S. Stephenson, G. B. Sands, I. J. LeGrice, H. Zhang, J. C. Jarvis, *et al.*, "Atrial fibrosis and atrial fibrillation: a computer simulation in the posterior left atrium," in *International Conference on Functional Imaging and Modeling of the Heart*, 2013, pp. 400-408.
- [33] J. Zhao, T. D. Butters, H. Zhang, A. J. Pullan, I. J. LeGrice, G. B. Sands, *et al.*, "An image-based model of atrial muscular architecture effects of structural anisotropy on electrical activation," *Circulation: Arrhythmia and Electrophysiology*, vol. 5, pp. 361-370, 2012.
- [34] J. Zhao, T. D. Butters, H. Zhang, I. J. LeGrice, G. B. Sands, and B. H. Small, "Image-based model of atrial anatomy and electrical activation: A computational platform for investigating atrial arrhythmia," *IEEE transactions on medical imaging*, vol. 32, pp. 18-27, 2013.
- [35] J. Zhao, B. J. Hansen, T. A. Csepe, P. Lim, Y. Wang, M. Williams, *et al.*, "Integration of high-resolution optical mapping and 3-dimensional micro-computed tomographic imaging to resolve the structural basis of atrial conduction in the human heart," *Circulation: Arrhythmia and Electrophysiology*, vol. 8, pp. 1514-1517, 2015.
- [36] P. Kirchhof and H. Calkins, "Catheter ablation in patients with persistent atrial fibrillation," *European Heart Journal*, p. ehw260, 2016.
- [37] G. Golds and F. Beg, "Computing the thickness of the ventricular heart wall from 3d mri images," in *Medical Imaging 2005: Image Processing*, 2005, pp. 1925-1933.
- [38] S. YEN HO, D. SANCHEZ-QUINTANA, J. A. Cabrera, and R. H. Anderson, "Anatomy of the left atrium: implications for radiofrequency ablation of atrial fibrillation," *Journal of cardiovascular electrophysiology*, vol. 10, pp. 1525-1533, 1999.
- [39] B. Fischl and A. M. Dale, "Measuring the thickness of the human cerebral cortex from magnetic resonance images," *Proceedings of the National Academy of Sciences*, vol. 97, pp. 11050-11055, 2000.
- [40] S. E. Jones, B. R. Buchbinder, and I. Aharon, "Three-dimensional mapping of cortical thickness using Laplace's Equation," *Human brain mapping*, vol. 11, pp. 12-32, 2000.
- [41] D. Sánchez-Quintana, J. A. Cabrera, V. Climent, J. Farré, M. C. De Mendonça, and S. Y. Ho, "Anatomic relations between the esophagus and left atrium and relevance for ablation of atrial fibrillation," *Circulation*, vol. 112, pp. 1400-1405, 2005.
- [42] D. M. Harrild and C. S. Henriquez, "A computer model of normal conduction in the human atria," *Circulation research*, vol. 87, pp. e25-e36, 2000.
- [43] A. Ahmad Bakir, A. Al Abed, M. C. Stevens, N. H. Lovell, and S. Dokos, "A Multiphysics Biventricular Cardiac Model: Simulations With a Left-Ventricular Assist Device," *Frontiers in physiology*, vol. 9, p. 1259, 2018.
- [44] E. Fares and W. Schröder, "A differential equation for approximate wall distance," *International journal for numerical methods in fluids*, vol. 39, pp. 743-762, 2002.